IEEE Photonics Journal
An IEEE Photonics Society Publication

Open Access

Multi-Layer Superimposed Transmission for Optical Wireless Scattering Communication

Volume 11, Number 5, October 2019

Guanchu Wang
Chen Gong
Zhimeng Jiang
Zhengyuan Xu

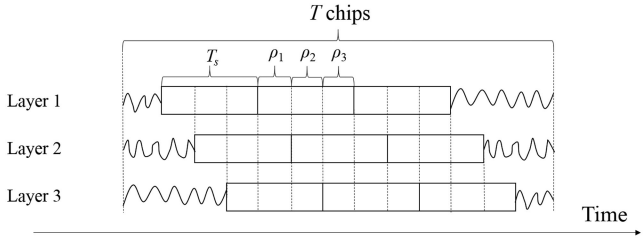

DOI: 10.1109/JPHOT.2019.2942652

IEEE photonics SOCIETY
IEEE

Multi-Layer Superimposed Transmission for Optical Wireless Scattering Communication

Guanchu Wang, Chen Gong, Zhimeng Jiang, and Zhengyuan Xu

Key Laboratory of Wireless-Optical Communications, Chinese Academy of Sciences, School of Information Science and Technology, University of Science and Technology of China, Hefei 230052, China

DOI:10.1109/JPHOT.2019.2942652

Manuscript received August 14, 2019; revised September 10, 2019; accepted September 17, 2019. Date of publication September 20, 2019; date of current version October 7, 2019. This work was supported in part by the National Key Research and Development Program of China under Grant 2018YFB1801904, in part by the Key Program of National Natural Science Foundation of China under Grant 61631018, in part by the Key Research Program of Frontier Sciences of CAS under Grant QYZDY-SSW-JSC003. This paper was presented in part at the Optical Wireless Communication workshop, Kansas City, MO, USA, May 2018. Corresponding author: Chen Gong. (e-mail: cgong821@ustc.edu.cn).

This paper has supplementary downloadable material available at http://ieeexplore.ieee.org, provided by the authors.

Abstract: We investigate the multi-layer superimposed transmission for optical wireless scattering communication where the symbol boundaries on different signal layers are not necessarily aligned in the time domain. We characterize the multi-layer transmission based on a hidden markov model, and propose approaches on the channel estimation as well as joint symbol detection and decoding. Finally, both simulations and experiments are conducted to evaluate the performance of the proposed approaches, and validate the feasibility of the proposed transmission and signal detection approaches.

Index Terms: NLOS scattering communication, superimposed transmission, hidden markov model, joint detection and decoding.

1. Introduction

Optical wireless communication can serve as an effective supplement of conventional radio-frequency (RF) communication, due to its potential large bandwidth and capacity [2]. It can be widely deployed in long range free-space communication, network communication, and device to device communication [3]. Furthermore, it can satisfy the RF silence requirements in many scenarios, for example the special areas in hospitals or battlefield, since it cause absolutely no electromagnetic radiation or electromagnetic interference. In some scenarios, the line of sight links are difficult to guarantee due to obstacles or the user mobility. Non-line of sight (NLOS) Ultra-violet (UV) scattering communication can be overcome this limitation, and it is more promising for outdoor communication under strong solar background because of negligible solar radiation in the UV spectrum [4].

Due to the extremely large path loss of NLOS channel link which has been studied by theoretical analysis [5], numerical simulation [6] and real experiments [7], [8], the technique of photon-

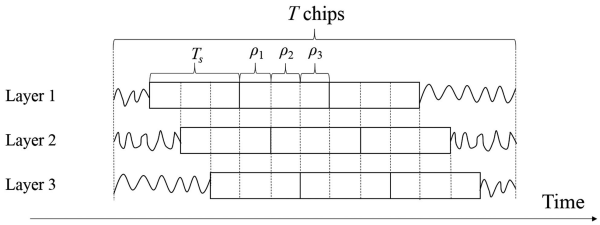

Fig. 1. Illustration for 3-layer superimposed transmission.

counting [9] has been widely applied to the receiver-side detection. Discrete Poisson channel model is both valid and precise enough for NLOS scattering communication based on photon-counting detection, which makes it feasible to theoretically investigate the receiver-side signal processing [10], [11]; and its preciseness has been verified by the experiments in [12], [13] as well as the realization of FPGA-based real-time scattering communication systems in [14].

The capacity of point-to-point continuous-time Poisson channel has been investigated in [15], [16], and the capacity of discrete-time Poisson channel has been derived in [17], [18]. Based on the Poisson channel model, several types of channel model such as Poisson fading, MIMO, interfering, broadcast, and multiple access channels have been studied in [19]–[23] and [24]–[26], respectively, in recent years. Other existing works on NLOS UV scattering communication based on the Poisson and extended channel model are the channel link gain with impulse response [27], [28], channel estimation with inter-symbol interference [29], signal detection with receiver diversity [30], and relay protocol [31].

In this work, we characterize multi-layer superimposed transmission in discrete Poisson channel, where the transmitted symbols in various layers are superimposed, and the symbol boundaries on different signal layers are not necessarily aligned. The proposed scenario can be characterized by hidden markov model (HMM) [32], [33]. For receiver-side signal processing, we propose channel estimation based on expectation-maximization (EM) algorithm [34], [35], and adopt Viterbi [36] and Bahl-Cocke-Jelinek-Raviv (BCJR) [37] algorithms for symbol detection. Furthermore, we propose iterative algorithm for maximum-likelihood/maximum a posteriori probability (ML/MAP) joint decoding [38], [39]. Finally, we conduct offline experiments to evaluate the performance of the proposed approaches. It is seen that based on the experimental measurements, the proposed approaches perform close to the simulation results with identical channel parameters.

The remainder of the paper is organized as follows. In Section 2, we characterize the superimposed NLOS scattering communication using HMM. In Section 3, we propose the EM-based channel estimation as well as joint symbol detection and decoding. Numerical and experimental results are given in Sections 4 and 5, respectively. Finally, we conclude this paper in Section 6.

2. System Model

We consider multi-layer superposition of NLOS optical wireless scattering communication. Different signal layers are superimposed at the transmitter, and jointly decoded at the receiver.

2.1 Superimposed Transmission Based on Discrete Poisson Asynchronous Channel

In this work, we consider a short range NLOS scattering communication system with on-off key (OOK) modulation, where the symbol rate is up to 1 Mbps, and the inter-symbol interference can be negligible. The overall transmission signal can be split into multiple signal layers which are superimposed possibly in an asynchronous manner, i.e., the symbols in different layers are not necessarily aligned. As shown in Fig. 1, the overall transmission can be split into L signal layers, denoted as layer $1, 2, \ldots, L$. Let M denote the number of transmitted symbols in each single layer; T_s denote the symbol duration; and $\rho_1, \rho_2, \ldots, \rho_L$ denote the normalized relative delay in terms of T_s

$\left(\sum_{i=1}^{L}\rho_i = 1\right)$, where ρ_i denotes the normalized delay between layer i and layer $i+1$, for $1 \le i \le L$ (here layer $L+1$ is equivalent to Layer 1).

In order to characterize the symbol duration offset in different signal layers, we divide the symbols in different signal layers into chips subjected to symbol boundaries, where the symbol detection is performed based on the received signal in each chip. The symbol misalignment and relative delay are illustrated in Fig. 1, where T denotes the number of overall chips and $T = ML + L - 1$.

Due to the weak received signal intensity of NLOS scattering communications, the received signal can be characterized by discrete photoelectrons, and can be described by the discrete Poisson channel model. Specifically, the number of detected photoelectrons within one symbol duration in the receiver-side satisfies the following Poisson distribution,

$$\mathbb{P}(N = n|\lambda) = \frac{\lambda^n}{n!}e^{-\lambda}, \tag{1}$$

where λ denotes the mean photon-number in each symbol duration determined by the transmission power P in the transmitter-side by $\lambda = \frac{\eta P}{\hbar \nu}$; η, h, v and ζ denote the quantum efficiency of the receiver-side detector including optical filter and photon detector, Planck's constant, the frequency of the optical field, and the path loss, respectively.

More specifically, let $\lambda_1, \lambda_2, \ldots, \lambda_L$ denote the mean one-symbol-duration photon-number, and $\boldsymbol{z}_1, \boldsymbol{z}_2, \ldots, \boldsymbol{z}_L$ denote the transmitted binary symbols in layers $1, 2, \ldots, L$, respectively, where $\boldsymbol{z}_i = [z_{i,1}, z_{i,2}, \ldots, z_{i,M}] \in \{0,1\}^M$; $z_{i,m}$ demotes the m-th symbol in layer i for $1 \le i \le L$ and $1 \le m \le M$; and the transmitted symbols are independent of each other. The number of detected photoelectrons N_t in the t-th chip for $1 \le t \le T$ satisfies the following Poisson distribution,

$$\mathbb{P}(N_t = n) = \frac{\tau_t^n}{n!}(\lambda_0 + \boldsymbol{\Lambda}^T \boldsymbol{S}_t)^n e^{-\tau_t(\lambda_0 + \boldsymbol{\Lambda}^T \boldsymbol{S}_t)}, \tag{2}$$

where $\boldsymbol{\Lambda} = [\lambda_1, \lambda_2, \ldots, \lambda_M]^T$; $\tau_t = \rho_{(t-1 \bmod M)+1}$; $\boldsymbol{S}_t = [z_{1,\lceil \frac{t}{L} \rceil}, z_{2,\lceil \frac{t-1}{L} \rceil}, \ldots, z_{L,\lceil \frac{t-L+1}{L} \rceil}]^T$; $z_{i,0} = 0$, $z_{i,M+1} = 0$ for $1 \le i \le L$; and λ_0 denotes the mean photon-number of background radiation photoelectrons in one symbol duration.

Proof: Please refer to Appendix 7.1. ■

2.2 Hidden Markov Model for Asynchronous Signal Superposition

Due to the overlap of different layers, the numbers of detected photoelectrons in adjacent chips are correlated with each other. In the t-th chip, N_t depends on $\boldsymbol{S}_t$, which depends on $\boldsymbol{S}_{t-1}$. Consequently, we can adopt HMM to characterize the signal model in the chip level.

We denote $\boldsymbol{S}_1, \boldsymbol{S}_2, \ldots, \boldsymbol{S}_T$ and $\boldsymbol{N}_T = [N_1, N_2, \ldots, N_T] \in \mathbb{N}^L$ as the state and observation sequences of the HMM, respectively, where $\boldsymbol{S}_t \in \mathscr{B}^L$, and $\mathscr{B}^L$ denotes the state space of the t-th chip given by

$$\mathscr{B}^L = \left\{ \sum_{i=1}^{L} \theta_i \boldsymbol{e}_i \mid \theta_i \in \{0,1\}, 1 \le i \le L \right\}, \tag{3}$$

where $\boldsymbol{e}_i$ denotes the i-th column of $L \times L$ identity matrix.

An HMM is determined by parameters $(\boldsymbol{\pi}_1, \boldsymbol{A}_t, \boldsymbol{B}_t)$, where $\boldsymbol{\pi}_1$, $\boldsymbol{A}_t$ and $\boldsymbol{B}_t$ denote the initial distribution, state transition matrix and observation emission matrix, respectively. Note that the initial state depends on the first symbol in the first layer, thus $\boldsymbol{\pi}_1$ is given by

$$\boldsymbol{\pi}_1 = \Big\{ q_1, 1-q_1, 0, 0, \ldots, 0 \Big\}, \tag{4}$$

where $q_i = \mathbb{P}(z_{i,j} = 1)$ denotes the prior possibility of transmitted symbols in signal layer i, which remains invariant in single layer due to the assumption that different types of transmission are allocated to different signal layers.

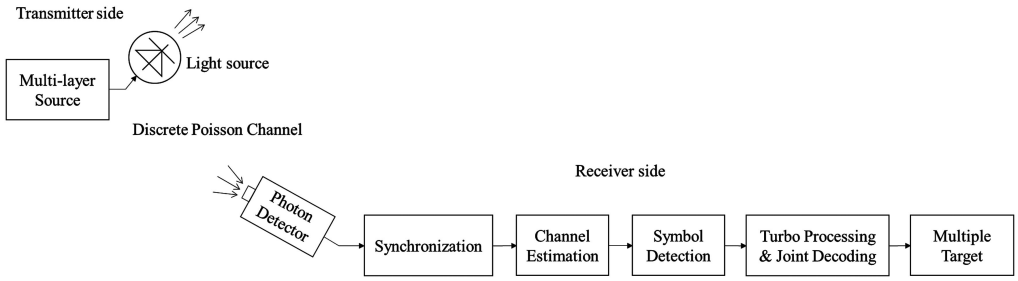

Fig. 2. Configuration of multi-layer communication system.

The state transition matrix is given by $\boldsymbol{A}_t = \left[a_{t,i,j} | \boldsymbol{s}_{t,i} \in \mathscr{B}^L, \boldsymbol{s}_{t+1,j} \in \mathscr{B}^L\right]$ for $1 \leq t < T$, where each element $a_{t,i,j}$ is given by

$$\begin{aligned} a_{t,i,j} &= \mathbb{P}(\boldsymbol{S}_{t+1} = \boldsymbol{s}_{t+1,j} | \boldsymbol{S}_t = \boldsymbol{s}_{t,i}) \\ &= q_k^{\boldsymbol{s}_{t+1,j} \cdot \boldsymbol{e}_k} (1 - q_k)^{1 - \boldsymbol{s}_{t+1,j} \cdot \boldsymbol{e}_k} \prod_{r \neq k} (\boldsymbol{s}_{t+1,j} \cdot \boldsymbol{e}_r) \odot (\boldsymbol{s}_{t,i} \cdot \boldsymbol{e}_r), \end{aligned} \tag{5}$$

and $k = (t \bmod L) + 1$; $\boldsymbol{s}_{t,i}, \boldsymbol{s}_{t+1,j} \in \mathscr{B}^L$ take values among all possible choices of $\boldsymbol{S}_t$ and $\boldsymbol{S}_{t+1}$, respectively; moreover, $\odot$ indicates binary logical XNOR; and $\boldsymbol{A}_t$ is cyclical of period L.

Proof: Please refer to Appendix 7.2. ■

The observation emission matrix is given by $\boldsymbol{B}_t = \left[b_{t,i,n+1} | \boldsymbol{s}_{t,i} \in \mathscr{B}^L, n \in \mathbb{N}\right]$, where based on Equation (2) each element $b_{t,i,n+1}$ is given by

$$\begin{aligned} b_{t,i,n+1} &= \mathbb{P}(N_t = n | \boldsymbol{S}_t = \boldsymbol{s}_{t,i}) \\ &= \frac{\tau_t^n}{n!} (\lambda_0 + \boldsymbol{\lambda}_{\boldsymbol{s}_{t,i}}) e^{-\tau_t (\lambda_0 + \boldsymbol{\lambda}_{\boldsymbol{s}_{t,i}})}, \end{aligned} \tag{6}$$

where $\boldsymbol{\lambda}_{\boldsymbol{s}_{t,i}} = \boldsymbol{\Lambda}^T \boldsymbol{s}_{t,i}$ denotes the mean photon-number of state $\boldsymbol{s}_{t,i}$.

2.3 System Configuration

We consider the whole system illustrated in Fig. 2. In the transmitter side, multiple data sources with potentially different prior probabilities are allocated to multiple signal layers; while in the receiver side, the digital signal processing consists of synchronization, channel estimation, symbol detection and joint decoding of error correction code. Based on the $(\boldsymbol{\pi}_1, \boldsymbol{A}_t, \boldsymbol{B}_t)$ HMM, we focus on the the last three modules of signal processing since the synchronization can be implemented by conventional approaches, e.g. [14].

3. Channel Estimation and Symbol Detection

We present the receiver-side signal processing including channel estimation, symbol detection as well as joint detection and decoding.

3.1 Channel Estimation Algorithm

The channel estimation is adopted to estimate $\hat{\boldsymbol{B}}_t$, which is equivalent to the estimation of $\hat{\lambda}_{\boldsymbol{s}_i}$ for $\boldsymbol{s}_i \in \mathscr{B}^L$. The maximum likelihood estimation can be obtained via inserting pilot sequences in all signal layers, however, the overhead will be non-negligible. In this work, the channel estimation can be performed based on pilot sequences on certain signal layers but not necessarily on all, which is called partial pilot-based channel estimation, as illustrated in Fig. 3. Without loss of generality, we assume to transmit pilot sequences $\boldsymbol{Z}^p = [\boldsymbol{z}_1^p, \boldsymbol{z}_2^p, \ldots, \boldsymbol{z}_{L_p}^p]$ in L_p layers, where $\boldsymbol{z}_i^p$

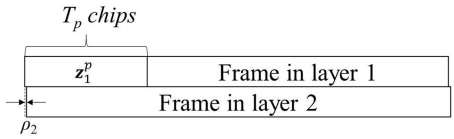

Fig. 3. Illustration of partial pilot-based channel estimation for $L = 2, L_p = 1$.

denotes the pilot sequence in layer i for $1 \le i \le L_p$ and $0 \le L_p < L$. Let $\boldsymbol{S}_1^p, \boldsymbol{S}_2^p, \ldots, \boldsymbol{S}_{T_p}^p$ denote the state sequence for channel estimation, where T_p denotes the number of chips. We have that $\boldsymbol{S}_t^p = [z^p_{1,\lceil \frac{t}{L} \rceil}, \ldots, z^p_{L_p,\lceil \frac{t-1}{L} \rceil}, z_{L_p+1,\lceil \frac{t-1}{L} \rceil}, \ldots, z_{L,\lceil \frac{t-L+1}{L} \rceil}]^T$, and $\hat{\boldsymbol{\Lambda}}$ is estimated based on EM algorithm. Let $\boldsymbol{N}^p = [N_1^p, N_2^p, \ldots, N_{T_p}^p]$ denote the number of received photoelectrons in each chip for channel estimation, where $\boldsymbol{N}^p$ is the observation sequence of $\boldsymbol{S}_t^p$ for $1 \le t \le T_p$. The estimation for $\hat{\boldsymbol{\Lambda}}$ is processed by V iterations, and in each iteration the updating rule is provided as follows.

E-step: In the vth iteration, based on the estimate result $\hat{\lambda}_{\boldsymbol{s}_i}^{(v-1)}$ in the $(v-1)$th iteration, the a posterior probability of $\boldsymbol{S}_t^p$ is given by

$$Q^{(v)}(\boldsymbol{S}_t^p = \boldsymbol{s}_i) = \mathbb{P}(\boldsymbol{S}_t^p = \boldsymbol{s}_i | \boldsymbol{N}^p, \lambda_{\boldsymbol{s}_i} = \hat{\lambda}_{\boldsymbol{s}_i}^{(v-1)}) = \frac{\mathbb{P}(\boldsymbol{N}^p, \boldsymbol{S}_t^p = \boldsymbol{s}_i | \lambda_{\boldsymbol{s}_i} = \hat{\lambda}_{\boldsymbol{s}_i}^{(v-1)})}{\sum_{\boldsymbol{s}_i \in \mathscr{B}^{L \setminus L_p}} \mathbb{P}(\boldsymbol{N}^p, \boldsymbol{S}_t^p = \boldsymbol{s}_i | \lambda_{\boldsymbol{s}_i} = \hat{\lambda}_{\boldsymbol{s}_i}^{(v-1)})}, \tag{7}$$

where $\mathscr{B}^{L \setminus L_p} = \left\{ \sum_{i=1}^{L_p} z^p_{i,\lceil \frac{t-i+1}{L} \rceil} \boldsymbol{e}_i + \sum_{i=L_p+1}^{L} \theta_i \boldsymbol{e}_i \mid \theta_i \in \{0, 1\}, L_p + 1 \le i \le L \right\}$, and

$$\mathbb{P}(\boldsymbol{N}^p, \boldsymbol{S}_t^p = \boldsymbol{s}_i | \lambda_{\boldsymbol{s}_i} = \hat{\lambda}_{\boldsymbol{s}_i}^{(v-1)}) = \frac{\left(\tau_t \hat{\lambda}_{\boldsymbol{s}_i}^{(v-1)}\right)^{N_t^p}}{N_t^p!} e^{-\tau_t \hat{\lambda}_{\boldsymbol{s}_i}^{(v-1)}}. \tag{8}$$

M-step: Given a posterior probability $Q^{(v)}(\boldsymbol{S}_t^p = \boldsymbol{s}_i)$ for the vth iteration, the ML-estimation for $\hat{\boldsymbol{\Lambda}}_T^{(v)} = \{\hat{\lambda}_{\boldsymbol{s}_i}^{(v)} | \boldsymbol{s}_i \in \mathscr{B}^{L \setminus L_p}\}$ is given by

$$\hat{\lambda}_{\boldsymbol{s}_j}^{(v)} = \frac{\sum_{t=1}^{T_p} Q^{(v)}(\boldsymbol{S}_t^p = \boldsymbol{s}_i) N_t^p}{\sum_{t=1}^{T_p} Q^{(v)}(\boldsymbol{S}_t^p = \boldsymbol{s}_i) \tau_t}, \tag{9}$$

where the preset initial $\hat{\boldsymbol{\Lambda}}^{(0)}$ must satisfy $\left(\hat{\lambda}_{\boldsymbol{s}_i}^{(0)} - \hat{\lambda}_{\boldsymbol{s}_j}^{(0)}\right)\left(\lambda_{\boldsymbol{s}_i} - \lambda_{\boldsymbol{s}_j}\right) > 0$ for $i \ne j$ and $\lambda_{\boldsymbol{s}_i} \ne \lambda_{\boldsymbol{s}_j}$.

Proof: Please refer to Appendix 7.3. ■

Since the dimension of matrix $\boldsymbol{B}_t$ is always $|\mathscr{B}^L|$ for $1 \le t \le T$, the complexity of estimation grows exponentially with L.

3.2 HMM-Based Symbol Detection

The symbol detection aims to detect state sequence $\boldsymbol{S}_T$ according to the observation sequence $\boldsymbol{N}_T$ and $(\boldsymbol{\pi}_1, \boldsymbol{A}_t, \boldsymbol{B}_t)$ of HMM. The trellis diagram for HMM is adopted to find the optimal state transition path maximizing the likelihood function or a posteriori probability. Fig. 4 illustrates the trellis diagram for $L = 3$, where each state $\boldsymbol{S}_t$ is expressed as $\{z_{k,\lceil \frac{t-k+1}{L} \rceil} | 1 \le k \le L\}$, and each branch between adjacent states corresponds to a non-zero element of $\boldsymbol{A}_t$. We adopt Viterbi and Bahl-Cocke-Jelinek-Raviv (BCJR) algorithms to maximize the likelihood function $\mathbb{P}(\boldsymbol{N}_T | \boldsymbol{S}_1, \ldots, \boldsymbol{S}_T)$ and a posteriori probability $\mathbb{P}(z_{k,i} | \boldsymbol{N}_T)$ for $1 \le k \le L$ and $1 \le i \le M$, respectively, and minimizes the error rate of sequence and symbol detection, respectively.

For Viterbi algorithm, we maximize the log-likelihood function of state sequence summarized as follows

$$\hat{\boldsymbol{S}}_1 \ldots, \hat{\boldsymbol{S}}_T = \arg\max \log \mathbb{P}(\boldsymbol{N}_T | \boldsymbol{S}_1, \ldots, \boldsymbol{S}_T) = \arg \max_{\boldsymbol{S}_t \in \mathscr{B}^L} \sum_{t=1}^{T} N_t \log \tau_t \lambda_{\boldsymbol{S}_t} - \tau_t \lambda_{\boldsymbol{S}_t}, \tag{10}$$

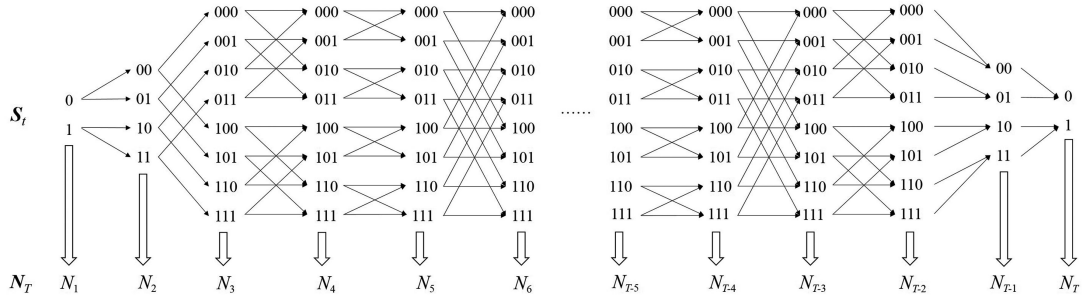

Fig. 4. The trellis diagram for $L = 3$.

where $\lambda_{\boldsymbol{S}_t}$ for $\boldsymbol{S}_t \in \mathscr{B}^L$ can be obtained from channel estimation.

Letting $\mathcal{L}(N_t|\boldsymbol{S}_t) = N_t \log \tau_t \lambda_{\boldsymbol{S}_t} - \tau_t \lambda_{\boldsymbol{S}_t}$, we have that $\mathcal{L}(\boldsymbol{N}_t|\boldsymbol{S}_t) = \mathcal{L}(N_t|\boldsymbol{S}_t) + \mathcal{L}(\boldsymbol{N}_{t-1}|\boldsymbol{S}_{t-1})$ for $2 \le t \le T$. Thus dynamic programming is adopted with the following updated equation

$$\max \mathcal{L}(\boldsymbol{N}_{t+1}|\boldsymbol{S}_t, \boldsymbol{S}_{t+1,j}) = \mathcal{L}(N_{t+1}|\boldsymbol{S}_{t+1,j}) + \max_{a_{i,j,t} \neq 0} \left\{ \mathcal{L}(\boldsymbol{N}_t|\boldsymbol{S}^{t-1}, \boldsymbol{S}_{t,i}) \right\}, \tag{11}$$

which is initialized by $\mathcal{L}(\boldsymbol{N}_1|\boldsymbol{S}_1) = \mathcal{L}(N_1|\boldsymbol{S}_1) \sim N_1 \log \tau_1(\lambda_0 + \lambda_{\boldsymbol{S}_1}) - \tau_1(\lambda_0 + \lambda_{\boldsymbol{S}_1})$. The detected symbol sequence can be retrieved via tracing back the optimal path.

For BCJR Algorithm, we maximize the posterior probability for each symbol $z_{k,i}$ for $1 \le k \le L$ and $1 \le i \le M$ as follows

$$\hat{z}_{i,j} = \arg\max \log \mathbb{P}(z_{k,i}|\boldsymbol{N}_T) = \arg\max \log \mathbb{P}(\boldsymbol{S}_{z_{k,i}}|\boldsymbol{N}_T) \sim \arg\max \log \mathbb{P}(\boldsymbol{S}_{z_{k,i}}, \boldsymbol{N}_T), \tag{12}$$

where $\boldsymbol{S}_{z_{k,i}} = \{\boldsymbol{S}_t | t = (i-1)L + k, (i-1)L + k + 1, \ldots, iL + k - 1\}$.

To obtain $\mathbb{P}(\boldsymbol{S}_{z_{k,i}}, \boldsymbol{N}_T)$, we define the following probability functions

$$\begin{aligned} \alpha_t(\boldsymbol{s}) &= \mathbb{P}(\boldsymbol{S}_t = \boldsymbol{s}, \boldsymbol{N}_t), \\ \beta_t(\boldsymbol{s}) &= \mathbb{P}(\boldsymbol{N}_{[t+1,T]}|\boldsymbol{S}_t = \boldsymbol{s}), \\ \gamma_t(\boldsymbol{v}, \boldsymbol{s}) &= \mathbb{P}(N_t, \boldsymbol{S}_t = \boldsymbol{s}|\boldsymbol{S}_{t-1} = \boldsymbol{v}), \end{aligned} \tag{13}$$

where $\boldsymbol{N}_{[a,b]} = \{N_t | a \le t \le b\}$. Note that we have

$$\mathbb{P}\left(\boldsymbol{S}_{z_{k,i}} = \$_{k,i}, \boldsymbol{N}_T\right) = \alpha_{(i-1)L+k}(\boldsymbol{s}_{(i-1)L+k}) \beta_{iL+k-1}(\boldsymbol{s}_{iL+k-1}) \prod_{t=(i-1)L+k}^{iL+k-2} \gamma_t(\boldsymbol{s}_t, \boldsymbol{s}_{t+1}), \tag{14}$$

where $\$_{k,i} = \{\boldsymbol{s}_t | (i-1)L + k \le t \le iL + k - 1\}$. Furthermore, we have that $\gamma_t(\boldsymbol{s}_{t-1,i}, \boldsymbol{s}_{t,j}, n) = a_{t-1,i,j} b_{t,j,n+1}$ for $\boldsymbol{s}_{t-1,i}, \boldsymbol{s}_{t,j} \in \mathscr{B}^L$ and $n \in \mathbb{N}$. Then, the calculations of $\alpha(\boldsymbol{s}_t)$ and $\beta(\boldsymbol{s}_t)$ are conducted according to the following recursive equations

$$\begin{aligned} \alpha_t(\boldsymbol{s}_t) &= \sum_{\boldsymbol{s}_{t-1} \in \mathscr{B}^L} \alpha_{t-1}(\boldsymbol{s}_{t-1}) \gamma_t(\boldsymbol{s}_{t-1}, \boldsymbol{s}_t), \\ \beta_t(\boldsymbol{s}_t) &= \sum_{\boldsymbol{s}_{t+1} \in \mathscr{B}^L} \beta_{t+1}(\boldsymbol{s}_{t+1}) \gamma_{t+1}(\boldsymbol{s}_t, \boldsymbol{s}_{t+1}). \end{aligned} \tag{15}$$

The initial values are $\alpha_1(\boldsymbol{s}_{1,i}) = \pi_1(\boldsymbol{s}_{1,i}) b_{i,1,N_1+1}$ for $\boldsymbol{s}_{1,i} \in \mathscr{B}^L$ and $\beta_T(\boldsymbol{s}_T) = \pi_T(\boldsymbol{s}_T)$ for $\boldsymbol{s}_T \in \mathscr{B}^L$, where π_1 is given by Equation (4); and $\pi_t(\boldsymbol{s}_{t+1,i}) = \mathbb{P}(\boldsymbol{S}_{t+1} = \boldsymbol{s}_{t+1,i})$ can be obtained by the following recursive equation,

$$\pi_t(\boldsymbol{s}_{t+1,i}) = \sum_{\boldsymbol{s}_{t,j} \in \mathscr{B}^L} a_{t,j,i} \pi_{t-1}(\boldsymbol{s}_{t,j}). \tag{16}$$

3.3 Joint Detection and Decoding

We adopt joint detection and decoding based on turbo processing. For ML and MAP decoding, the log-likelihood ratio (LLR) and log-aposterior ratio (LAR) are adopted as the input soft information to the soft channel decoder, respectively. Let $LLR^{(v)}_{z_{k,i}}$ and $LAR^{(v)}_{z_{k,i}}$ denote the log-likelihood ratio and log-aposterior-ratio of $z_{k,i}$ after the v-th iteration, respectively. Typically each iteration of the turbo processing consists of one ML/MAP symbol detection operation followed by V channel decoding iterations.

For the ML-decoding, the initial LLR values are obtained by Viterbi algorithm as follows,

$$LLR^{(0)}_{z_{k,i}} = \log \frac{\mathbb{P}(\boldsymbol{N}_T|z_{k,i}=1)}{\mathbb{P}(\boldsymbol{N}_T|z_{k,i}=0)} = \sum_{t=(i-1)L+k}^{iL+k-1} \log \frac{\mathbb{P}(N_t|z_{k,i}=1)}{\mathbb{P}(N_t|z_{k,i}=0)}, \tag{17}$$

and the LLR of the i-th transmitted symbol in layer k in the v-th iteration is calculated by

$$LLR^{(v)}_{z_{k,i}} = \log \frac{\mathbb{P}(\boldsymbol{N}_T|z_{k,i}=1)}{\mathbb{P}(\boldsymbol{N}_T|z_{k,i}=0)} = \sum_{t=(i-1)L+k}^{iL+k-1} \log \frac{\mathbb{E}_{z_{k,i}=1}\mathbb{P}(N_t|\boldsymbol{S}_t=\boldsymbol{s}_t)}{\mathbb{E}_{z_{k,i}=0}\mathbb{P}(N_t|\boldsymbol{S}_t=\boldsymbol{s}_t)}, \tag{18}$$

where the expectation $\mathbb{E}_{z_{k,i}=\theta}[\bullet]$ for $\theta \in \{0,1\}$ is calculated based on a posterior probabilities by the $(v-1)$th iteration of channels in $\mathcal{L}\setminus k$ as follow,

$$\mathbb{E}_{\boldsymbol{s}_t\in\mathcal{S}_{z_{k,i}=\theta}}[\bullet] = \sum_{\boldsymbol{s}_t\in\mathcal{S}_{z_{k,i}=\theta}} \prod_{j\in\mathcal{L}\setminus k} \mathbb{P}^{1-z_{j,\lceil\frac{t-j+1}{L}\rceil}}_{(v-1)}\left(z_{j,\lceil\frac{t-j+1}{L}\rceil}=0|N_t\right) \mathbb{P}^{z_{j,\lceil\frac{t-j+1}{L}\rceil}}_{(v-1)}\left(z_{j,\lceil\frac{t-j+1}{L}\rceil}=1|N_t\right)[\bullet]; \tag{19}$$

and $\mathcal{S}_{z_{k,i}=\theta} = \{\boldsymbol{s}_t|\boldsymbol{e}_k^T\cdot\boldsymbol{s}_t=\theta|(i-1)L+k\le t\le iL+k-1\}$; $z_{j,\lceil\frac{t-j+1}{L}\rceil} = \boldsymbol{e}_j^T\cdot\boldsymbol{s}_t$; and the a posterior probability of $z_{j,\lceil\frac{t-j+1}{L}\rceil}$ after the $(v-1)$-th iteration is given by

$$\mathbb{P}_{(v-1)}\left(z_{j,\lceil\frac{t-j+1}{L}\rceil}=0|N_t\right) = 1-\mathbb{P}_{(v-1)}\left(z_{j,\lceil\frac{t-j+1}{L}\rceil}=1|N_t\right) = \frac{1}{1+\exp\left(\frac{q_j}{1-q_j}LLR^{(v-1)}_{j,\lceil\frac{t-j+1}{L}\rceil}\right)}. \tag{20}$$

For MAP-decoding, the initial LAR is determined by BLJR detection as follows

$$LAR^{(0)}_{z_{k,i}} = \log \frac{\mathbb{P}(z_{k,i}=1|\boldsymbol{N}_T)}{\mathbb{P}(z_{k,i}=0|\boldsymbol{N}_T)}; \tag{21}$$

and the LAR of symbol $z_{k,i}$ from the v-th iteration is given by

$$\begin{aligned} LAR^{(v)}_{z_{k,i}} &= \log \frac{\mathbb{P}_{(v-1)}\left(z_{j,\lceil\frac{t-j+1}{L}\rceil}=1|\boldsymbol{N}_T\right)}{\mathbb{P}_{(v-1)}\left(z_{j,\lceil\frac{t-j+1}{L}\rceil}=0|\boldsymbol{N}_T\right)} = \log \frac{\mathbb{P}\left(\boldsymbol{N}_T|z_{k,i}=1\right)}{\mathbb{P}\left(\boldsymbol{N}_T|z_{k,i}=0\right)} + \log \frac{\mathbb{P}(z_{k,i}=1)}{\mathbb{P}(z_{k,i}=0)} \\ &= LLR^{(v-1)}_{z_{k,i}} + \log \frac{q_k}{1-q_k}, \end{aligned} \tag{22}$$

where $LLR^{(v-1)}_{z_{k,i}}$ is computed according to Equations (18) and (19). Furthermore, the a posterior probability of MAP-decoding is given by

$$\mathbb{P}_{(v-1)}\left(z_{j,\lceil\frac{t-j+1}{L}\rceil}=0|N_t\right) = 1-\mathbb{P}_{(v-1)}\left(z_{j,\lceil\frac{t-j+1}{L}\rceil}=1|N_t\right) = \frac{1}{1+\exp\left(LAR^{(v-1)}_{j,\lceil\frac{t-j+1}{L}\rceil}\right)}. \tag{23}$$

The calculation of Equations (10), (12) and (19) depends on the enumeration of $\mathscr{B}^L$ and $1\le t\le T$, hence, the complexity of joint detection and decoding grows exponentially with L, and linearly with T.

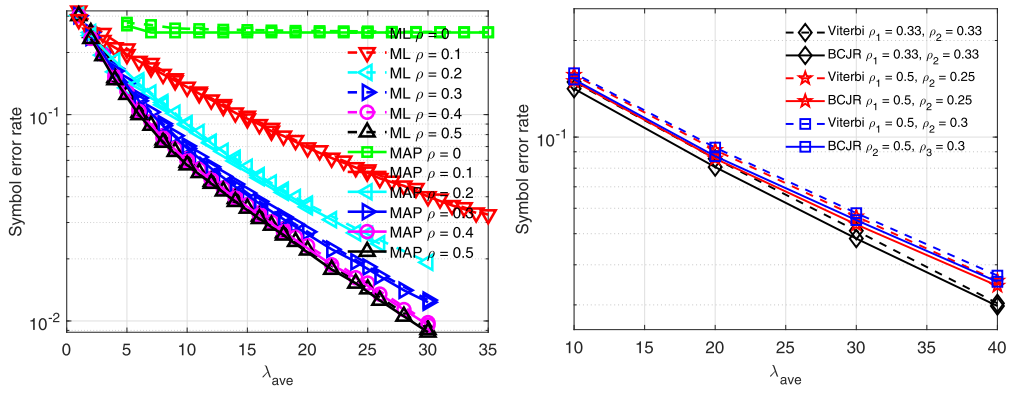

(a) The number of signal layer L=2. (b) The number of signal layer L=3.

Fig. 5. The symbol error rate of joint detection.

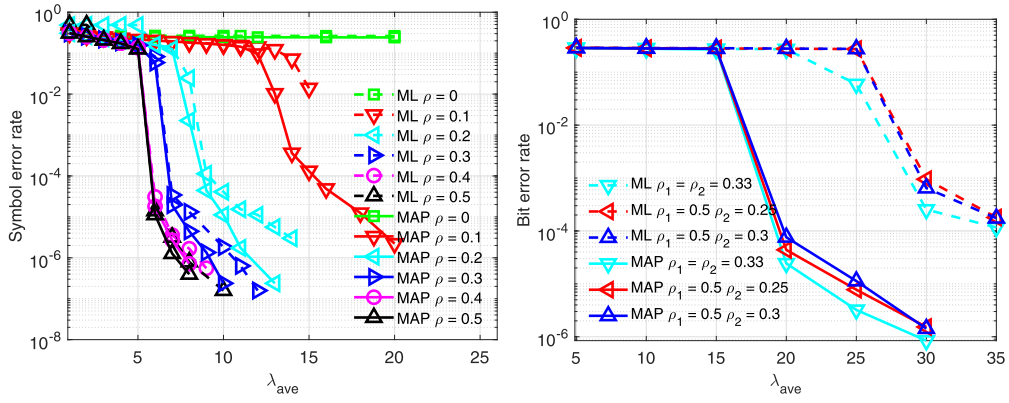

(a) The number of signal layer L=2. (b) The number of signal layer L=3.

Fig. 6. The bit error rate of joint detection and decoding with (12620, 6310) LDPC code.

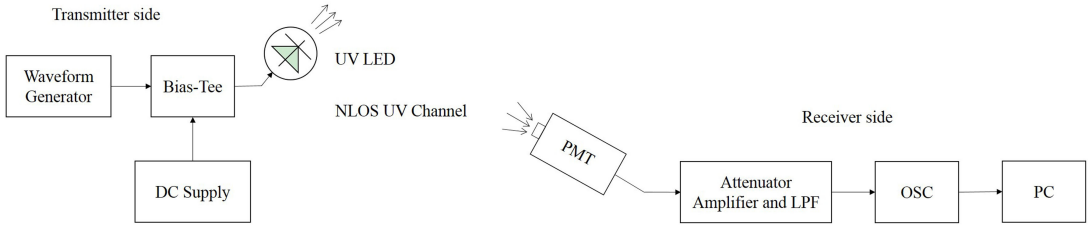

Fig. 7. Diagram of the experimental superimposed communication system.

4. Simulation of Joint Detection and Decoding

We assume that $\lambda_0 = 0.01$ and $\lambda_i = \lambda_{ave}$ for $1 \leq i \leq L$, and simulate that around 10^7 symbols are transmitted under 1 Mbps in our computers. The average symbol error rates for $L = 2$ and $L = 3$ of joint detection versus λ_{ave} are illustrated in Figures 5(a) and 5(b), respectively. Furthermore, we adopt a (12620, 6310) LDPC code for each signal layer, where the parity check matrix construction and low-complexity message pass decoding follow [40], [41] and [42]. We simulate that around 10^3 frames are transmitted under 1 Mbps and each frame consists of 12620 bits. The average bit error rates for $L = 2$ and $L = 3$ by joint detection and decoding versus λ_{ave} are shown in Figures 6(a) and 6(b), respectively.

TABLE 1
Specification of Device for Experiment

UV LED	Model	TO-3zz PO#2036
	Wavelength	280nm
	DC current	36mA
	DC voltage	11.818V
Optical filter	Peak transmission	28.2%
	Aperture size	Φ31.5mm $\times$28.3mm
PMT	Model	R7154
	Spectral response	160nm $\sim$ 320nm
	Dark counts	<10 per second
	Detection bandwidth	>200MHz

According to Figures 6(a) and 6(b), the bit error rate of LDPC decoding reaches 10^{-6}, which can meet the need of most practical systems. Besides, for $L = 2$, $\rho = 0$ has the highest error rate and $\rho = 0.5$ has the lowest error rate for both detection and decoding. The reason is the minimum achievable rate for $\rho = 0$ and the maximum achievable rate for $\rho = 0.5$, according to [1] and Fig. 11 in Appendix 7.4. Moreover, for two-layer transmission, in order to maintain the bit error rate lower than 10^{-6}, the receiver-side λ_{ave} should be larger than 15, meanwhile the relative delay should be in the range of $0.2 \leq \rho \leq 0.7$; for three-layer transmission, to maintain the bit error rate lower than 10^{-6}, the receiver-side λ_{ave} must be larger than 30, and the relative delays of two of the signal layers should be in the range of $0.33 \leq \rho_1 \leq 0.66$ and $0.25 \leq \rho_2 \leq 0.75$.

5. Experimental Results for 2-Layer-Superimposed Transmission

We conduct offline experiments on the 2-layer-superposition transmission for optical wireless scattering communication to experimentally evaluate the proposed joint detection and decoding. At the transmitter side, a waveform generator is adopted to produce OOK signals. A Bias-Tee is employed to combine the AC and DC signals to drive the UV LED. At the receiver side, a photomultiplier tube (PMT) is employed as the photon-detector, which is integrated with an optical filter in a sealed box. The UV signal of wavelength around 280nm can be detected, while the background radiation of other wavelengths is blocked. The PMT output signal is attenuated by an attenuator, amplified by an amplifier, and then filtered by a low-pass filter, which is then sampled by the oscilloscope. Finally, the photon counting processing, HMM-based MAP joint detection and decoding are realized in the received-side personal computer (PC) based on the sampled waveforms from the oscilloscope. Table 1 shows the specification of experimental equipment, and Figures 7, 8(a) and 8(b) illustrate the entire experimental block diagram and the test bed realizations, respectively.

In the experiment, the background radiation intensity is around 150 photoelectrons per second in the indoor environment ($\lambda_0 \approx 1.5 \times 10^{-4}$). The OOK data rate is 1 Mbps, and the data length is 12620 bits per block with totally 1000 blocks (1.262×10^7 random bits). We control the transmitted signal power such that the mean number of detected photons falls into the regime of interest given by the simulation results. Furthermore, we adopt the following parameters for two signal layers: symbol duration $T_s = 1$ μs; $\rho = 0.5$; uniform power to the 2 signal layers ($\lambda_1 = \lambda_2 = \lambda_{ave}$); the same parity check matrix construction and decoding algorithm of LDPC codes as those in simulation; and the uniform prior probabilities for $0 - 1$ symbols.

We experimentally evaluate channel estimation for $L = 2$, $\rho_1 = 0.5$, where we exploit a 255-bit m sequence as a pilot sequence $\boldsymbol{z}^p$ in the head of each frame (The ratio between pilot sequences and frame length is around 0.02). For $L_p = 1$, $\boldsymbol{z}_1^p = \boldsymbol{z}^p$; and for $L_p = 2$, $\boldsymbol{z}_1^p = \boldsymbol{z}_2^p = \boldsymbol{z}^p$. The performance of channel estimation versus the number of iterations is illustrated in Fig. 9(a), where the result of $L_p = 2$ is from the ML estimation. It is implied that real time estimation for both $L_p = 0$ and 1 can

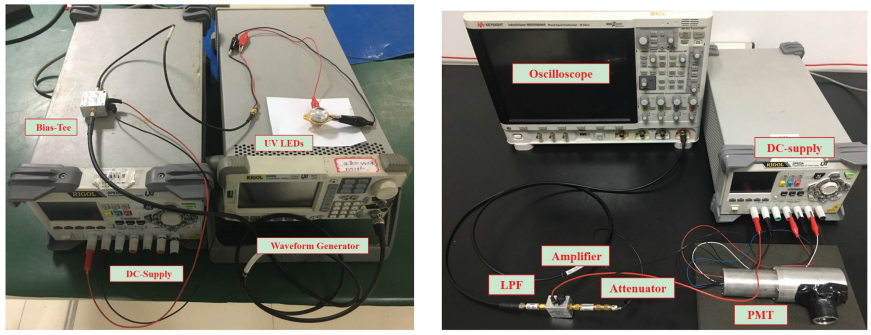

(a) Demonstration of the transmitter-side test bed. (b) Demonstration of the receiver-side test bed.

Fig. 8. Demonstration of the transmitter-side and receiver-side test beds.

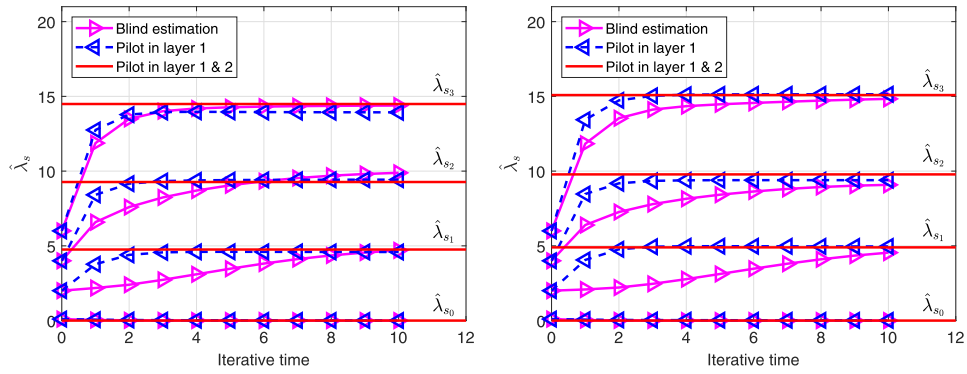

(a) Convergence of channel estimation from experiments. (b) Convergence of channel estimation from simulations.

Fig. 9. Convergence of channel estimation from both experiments and simulations.

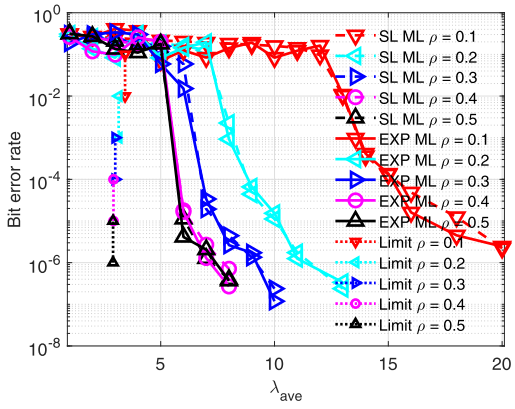

Fig. 10. The average bit error rate of 2-layer superimposed communication from simulation and experimental measurements.

converge to the ML solution; and assisted by the pilot sequence, the convergency of $L_p = 1$ is faster than $L_p = 0$. Furthermore, higher λ_{s_i} with large receiver-side SNR can lead to faster convergence, which is close to the simulation result on the channel estimation with the same system parameters, as shown in Fig. 9(b).

Moreover, the MAP detection with and without LDPC code (denoted as EXP) is evaluated in Fig. 10, where the simulation results with the same channel parameters (denoted as SL) is plotted for comparison. It is seen that the experimental results on the channel estimation, symbol detection

and joint detection/decoding are close to the simulation results, which illustrates the feasibility of the proposed channel estimation and signal detection approaches in real communication scenarios. Furthermore, according to [1], we calculate the the achievable transmission rate and plot the Shannon limit of $\rho = 0.1$ to 0.5 in Fig. 10 for comparison. Large gap can be observed for $\rho = 0.1$ to 0.3 since the codes are not optimized for the multi-layer Poisson channel. The validity of proposed algorithms of joint detection and decoding can be proved by the cases of $\rho = 0.4$ and 0.5, where around 2.34 dB gap to the Shannon limit is observed, and the gaps to the Shannon limits can be further reduced via codes optimization.

6. Conclusion

We have proposed multi-layer transmission for optical wireless scattering communication based on HMM, and investigate the receiver-side signal processing including EM-based estimation as well as joint detection and decoding. The performance of the proposed approaches are verified by numerical results. Moreover, for two- and three-layer transmission, both simulation and experimental results are employed to validate the feasibility of the proposed algorithms.

Appendix

7.1 Proof of the Distribution of One-Chip-duration Photon-Number

According to the discrete Poisson Channel, given the m-th transmitted symbol $z_{i,m}$ in layer i and the mean one-symbol-duration photon-number λ_i for $1 \leq i \leq L$, the number of detected photoelectrons n within one symbol duration in layer i satisfies the following Poisson distribution,

$$\mathbb{P}(n|z_{i,m}) = \frac{(\lambda_0 + z_{i,m}\lambda_i)^n}{n!} e^{-(\lambda_0 + z_{i,m}\lambda_i)}. \tag{24}$$

Since the channel has been split into L layers, the overall one-symbol-duration photon-number equals the summation of that of each layer. Considering that the mean one-chip-duration photon-number is τ_t times that of each symbol, the number of detected photoelectrons N_t in the t-th chip satisfies the following Poisson distribution,

$$\mathbb{P}(N_t = n|x_1, x_2, \ldots, x_L) = \frac{\left[\tau_t(\lambda_0 + \sum_{i=1}^{L} x_i\lambda_i)\right]^n}{n!} e^{-\tau_t(\lambda_0 + \sum_{i=1}^{L} x_i\lambda_i)}, \tag{25}$$

where $x_1, x_2, \ldots, x_L$ denotes the transmitted symbol in the t-th chip from layers $1, 2, \ldots, L$, respectively.

Due to the relationship between t (the subscript of τ_t) and m (the second subscript of $z_{i,m}$) for $1 \leq i \leq L$, the transmitted symbols in the t-th chip from layers $1, 2, \ldots, L$ are $z_{1,\lceil \frac{t}{L} \rceil}, z_{2,\lceil \frac{t-1}{L} \rceil}, \ldots, z_{L,\lceil \frac{t-L+1}{L} \rceil}$, respectively, and Equation (25) is equivalent to Equation (2).

7.2 Proof of State Transition Matrix

Note that $\lceil \frac{t+1-k+1}{L} \rceil = \lceil \frac{t-k+1}{L} \rceil + 1$ for $k = (t \bmod L) + 1$, and $\lceil \frac{t+1-r+1}{L} \rceil = \lceil \frac{t-r+1}{L} \rceil$ for $r \neq k$, the r-th element of $\boldsymbol{S}_t = [z_{1,\lceil \frac{t}{L} \rceil}, z_{2,\lceil \frac{t-1}{L} \rceil}, \ldots, z_{L,\lceil \frac{t-L+1}{L} \rceil}]^T$ and $\boldsymbol{S}_{t+1} = [z_{1,\lceil \frac{t+1}{L} \rceil}, z_{2,\lceil \frac{t}{L} \rceil}, \ldots, z_{L,\lceil \frac{t-L+2}{L} \rceil}]^T$ must satisfy $z_{r,\lceil \frac{t-r+1}{L} \rceil} = z_{r,\lceil \frac{t+1-r+1}{L} \rceil}$ for $r \neq k$. Consequently, The state transition probability $\mathbb{P}(\boldsymbol{S}_{t+1} = \boldsymbol{s}_{t+1,j}|\boldsymbol{S}_t = \boldsymbol{s}_{t,i}) = 0$, if $z_{r,\lceil \frac{t-r+1}{L} \rceil} \neq z_{r,\lceil \frac{t+1-r+1}{L} \rceil}$; and $\mathbb{P}(\boldsymbol{S}_{t+1} = \boldsymbol{s}_{t+1,j}|\boldsymbol{S}_t = \boldsymbol{s}_{t,i}) = \mathbb{P}(z_{k,\lceil \frac{t+1-k+1}{L} \rceil}|z_{k,\lceil \frac{t-k+1}{L} \rceil})$. Furthermore, $z_{k,\lceil \frac{t+1-k+1}{L} \rceil}$ is independent of $z_{k,\lceil \frac{t-k+1}{L} \rceil}$, hence we have that $\mathbb{P}(z_{k,\lceil \frac{t+1-k+1}{L} \rceil}|z_{k,\lceil \frac{t-k+1}{L} \rceil}) = q_k^{z_{k,\lceil \frac{t+1-k+1}{L} \rceil}}(1-q_k)^{1-z_{k,\lceil \frac{t+1-k+1}{L} \rceil}}$. Since $z_{i,\lceil \frac{t-i+1}{L} \rceil} = \boldsymbol{S}_t \cdot \boldsymbol{e}_i$ for $1 \leq i \leq L$, $z_{r,\lceil \frac{t-r+1}{L} \rceil} \neq z_{r,\lceil \frac{t+1-r+1}{L} \rceil}$ is equivalent with $(\boldsymbol{s}_{t+1,j} \cdot \boldsymbol{e}_r) \odot (\boldsymbol{s}_{t,i} \cdot \boldsymbol{e}_r) = 0$, and $\mathbb{P}(\boldsymbol{S}_{t+1} = \boldsymbol{s}_{t+1,j}|\boldsymbol{S}_t = \boldsymbol{s}_{t,i})$ can be simplified into Equation (5).

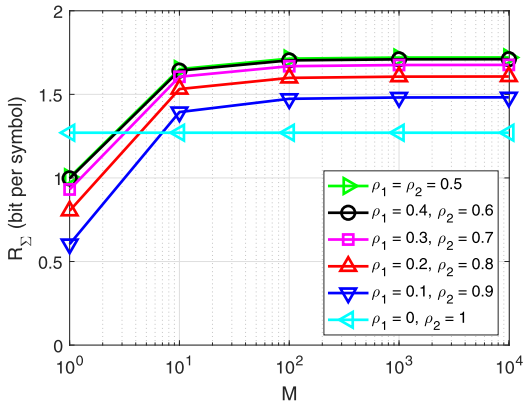

Fig. 11. The achievable rate of 2-layer transmission.

7.3 Derivation of $\hat{\Lambda}^{(v)}$ in the M-Step of Channel Estimation

The likelihood function is given by

$$\mathcal{L}(\boldsymbol{N}^p|\lambda_{\boldsymbol{s}_i}=\hat{\lambda}_{\boldsymbol{s}_i}^{(v)}) = \sum_{t=1}^{T_p}\log\sum_{\boldsymbol{s}_i\in\mathscr{B}^{L\setminus L_p}}\mathbb{P}(\boldsymbol{N}^p,\boldsymbol{S}_t^p=\boldsymbol{s}_i|\lambda_{\boldsymbol{s}_i}=\hat{\lambda}_{\boldsymbol{s}_i}^{(v)})$$
$$\geq \sum_{t=1}^{T_p}\sum_{\boldsymbol{s}_i\in\mathscr{B}^{L\setminus L_p}} Q^{(v)}(\boldsymbol{S}_t^p=\boldsymbol{s}_i)\log\frac{\mathbb{P}(\boldsymbol{N}^p,\boldsymbol{S}_t^p=\boldsymbol{s}_i|\lambda_{\boldsymbol{s}_i}=\hat{\lambda}_{\boldsymbol{s}_i}^{(v)})}{Q^{(v)}(\boldsymbol{S}_t^p=\boldsymbol{s}_i)}. \tag{26}$$

Letting $\tilde{\mathcal{L}}^{(v)}(\boldsymbol{N}^p|\lambda_{\boldsymbol{s}_i}=\hat{\lambda}_{\boldsymbol{s}_i}^{(v)})$ denote the last term of above inequality, we have that

$$\tilde{\mathcal{L}}^{(v)}(\boldsymbol{N}^p|\lambda_{\boldsymbol{s}_i}=\hat{\lambda}_{\boldsymbol{s}_i}^{(v)}) \sim \sum_{t=1}^{T_p}\sum_{\boldsymbol{s}_i\in\mathscr{B}^{L\setminus L_p}} Q^{(v)}(\boldsymbol{S}_t^p=\boldsymbol{s}_i)\Big(N_t^p\log\tau_t\hat{\lambda}_{\boldsymbol{s}_i}^{(v)}-\log N_t^p!-\tau_t\hat{\lambda}_{\boldsymbol{s}_i}^{(v)}\Big). \tag{27}$$

Hence, the partial derivative of likelihood function is given by

$$\frac{\partial}{\partial\lambda_{\boldsymbol{s}_i}^{(v)}}\tilde{\mathcal{L}}^{(v)}(\boldsymbol{N}^p=\boldsymbol{n}|\lambda_{\boldsymbol{s}_i}=\hat{\lambda}_{\boldsymbol{s}_i}^{(v)}) = \sum_{t=1}^{T_p} Q^{(v)}(\boldsymbol{S}_t^p=\boldsymbol{s}_i)\left(\frac{N_t^p}{\hat{\lambda}_{\boldsymbol{s}_i}^{(v)}}-\tau_t\right). \tag{28}$$

Letting $\frac{\partial}{\partial\lambda_{\boldsymbol{s}_j}}\mathcal{L}(\boldsymbol{N}^p=\boldsymbol{n}|\lambda_{\boldsymbol{s}_j}=\hat{\lambda}_{\boldsymbol{s}_j}^{(v)})=0$, we have that

$$\hat{\lambda}_{\boldsymbol{s}_j}^{(v)} = \arg\max\tilde{\mathcal{L}}^{(v)}(\boldsymbol{N}^p=\boldsymbol{n}|\lambda_{\boldsymbol{s}_i}=\hat{\lambda}_{\boldsymbol{s}_i}^{(v)}) = \frac{\sum_{t=1}^{T_p}Q^{(v)}(\boldsymbol{S}_t^p=\boldsymbol{s}_i)N_t^p}{\sum_{t=1}^{T_p}Q^{(v)}(\boldsymbol{S}_t^p=\boldsymbol{s}_i)\tau_t}. \tag{29}$$

7.4 The Achievable Rate of 2-Layer Transmission for $0 \leq \rho \leq 0.5$ Versus Frame Length

According to [1], the numerical results of achievable rate is given in Fig. 11, which implies that the achievable rate attains minimum for $\rho = 0$, only 1.25 bit per symbol; and reaches maximum for $\rho = 0.5$, up to 1.75 bit per symbol, which can justify the tendency of simulated symbol/bit error rate as ρ change from 0 to 0.5.

References

[1] G. Wang, C. Gong, Z. Jiang, and Z. Xu, "Characterization on asynchronous multiple access in non-line of sight scattering communication," in *Proc. IEEE Int. Conf. Commun. Workshops*, Kansas City, MO, USA, May 2018, pp. 1–6.

[2] H. Elgala, R. Mesleh, and H. Haas, "Indoor optical wireless communication: Potential and state-of-the-art," *IEEE Commun. Mag.*, vol. 49, no. 9, pp. 56–62, Sep. 2011.

[3] C. Gabriel, M.-A. Khalighi, S. Bourennane, P. Leon, and V. Rigaud, "Monte-Carlo-based channel characterization for underwater optical communication systems," *J. Opt. Commun. Netw.*, vol. 5, no. 1, pp. 1–12, Jan. 2013.

[4] Z. Xu and B. M. Sadler, "Ultraviolet communications: Potential and state-of-the-art," *IEEE Commun. Mag.*, vol. 46, no. 5, pp. 67–73 May 2008.

[5] C. Xu, H. Zhang, and J. Cheng, "Effects of haze particles and fog droplets on NLOS ultraviolet communication channels," *Opt. Exp.*, vol. 23, no. 18, pp. 23259–23269, 2015.

[6] Y. Sun and Y. Zhan, "Closed-form impulse response model of non-line-of-sight single-scatter propagation," *J. Opt. Soc. Amer. A*, vol. 33, no. 4, pp. 752–757, 2016.

[7] N. Raptis, E. Pikasis, and D. Syvridis, "Power losses in diffuse ultraviolet optical communications channels," *Opt. Lett.*, vol. 41, no. 18, pp. 4421–4424, 2016.

[8] K. Wang, C. Gong, D. Zou, and Z. Xu, "Turbulence channel modeling and non-parametric estimation for optical wireless scattering communication," *IEEE/OSA J. Lightwave Technol.*, vol. 35, pp. 2746–2756, Jul. 2017.

[9] D. Zou, C. Gong, K. Wang, and Z. Xu, "Characterization on practical photon counting receiver in optical scattering communication," *IEEE Trans. Commun.*, vol. 67, no. 3, pp. 2203–2217, Mar. 2019.

[10] X. Liu, C. Gong, and Z. Xu, "Sequential detection for optical wireless scattering communication," *IEEE/OSA J. Opt. Commun. Netw.*, vol. 9, no. 9, pp. D86–D95, Sep. 2017.

[11] D. Zou, C. Gong, and Z. Xu, "Signal detection under short-interval sampling of continuous waveforms for optical wireless scattering communication," *IEEE Trans. Wireless Commun.*, vol. 17, no. 5, pp. 3431–3443, May 2018.

[12] G. Chen, F. Abou-Galala, Z. Xu, and B. M. Sadler, "Experimental evaluation of LED-based solar blind NLOS communication links," *Opt. Exp.*, vol. 16, pp. 15059–15068, Sep. 2008.

[13] G. Chen, Z. Xu, H. Ding, and B. M. Sadler, "Path loss modeling and performance trade-off study for short-range non-line-of-sight ultraviolet communications," *Opt. Exp.*, vol. 17, pp. 3929–3940, Mar. 2009.

[14] G. Wang, K. Wang, C. Gong, D. Zou, Z. Jiang, and Z. Xu, "A 1 Mbps real-time NLOS UV scattering communication system with receiver diversity over 1 km," *IEEE Photon. J.*, vol. 10, no. 2, Apr. 2018, Art. no. 7903013.

[15] A. D. Wyner, "Capacity and error exponent for the direct detection photon channel. I-II," *IEEE Trans. Inf. Theory*, vol. 34, no. 6, pp. 1449–1461, Jun. 1988.

[16] M. R. Frey, "Information capacity of the Poisson channel," *IEEE Trans. Inf. Theory*, vol. 37, no. 2, pp. 244–256, Mar. 1991.

[17] A. Lapidoth and S. M. Moser, "On the capacity of the discrete-time Poisson channel," *IEEE Trans. Inf. Theory*, vol. 55, no. 1, pp. 303–322, Jan. 2009.

[18] A. Lapidoth, J. H. Shapiro, V. Venkatesan, and L. Wang, "The discrete-time Poisson channel at low input powers," *IEEE Trans. Inf. Theory*, vol. 57, no. 6, pp. 3260–3272, Jun. 2011.

[19] K. Chakraborty and P. Narayan, "The Poisson fading channel," *IEEE Trans. Inf. Theory*, vol. 53, no. 7, pp. 2349–2364, Jul. 2007.

[20] K. Chakraborty, S. Dey, and M. Franceschetti, "Outage capacity of MIMO Poisson fading channels," *IEEE Trans. Inf. Theory*, vol. 54, no. 11, pp. 4887–4907, Nov. 2008.

[21] L. Lai, Y. Liang, and S. S. Shitz, "On the capacity bounds for Poisson interference channels," *IEEE Trans. Inf. Theory*, vol. 61, no. 1, pp. 223–238, Jan. 2015.

[22] H. Kim, B. Nachman, and A. El Gamal, "Superposition coding is almost always optimal for the Poisson broadcast channel," *IEEE Trans. Inf. Theory*, vol. 62, no. 4, pp. 1782–1794, Apr. 2016.

[23] G. Wang, C. Gong, and Z. Xu, "Signal characterization for multiple access non-line of sight scattering communication," *IEEE Trans. Commun.*, vol. 66, pp. 4138–4154, Sep. 2018.

[24] N. Mehravari and T. Berger, "Poisson multiple-access contention with binary feedback," *IEEE Trans. Inf. Theory*, vol. 30, no. 5, pp. 745–751, May 1984.

[25] A. Lapidoth and S. Shamai, "The Poisson multiple-access channel," *IEEE Trans. Inf. Theory*, vol. 44, no. 2, pp. 488–501, Feb. 1998.

[26] S. I. Bross, M. V. Burnashev, and S. Shamai, "Error exponents for the two-user Poisson multiple-access channel," *IEEE Trans. Inf. Theory*, vol. 47, no. 5, pp. 1999–2016, May 2001.

[27] H. Ding, G. Chen, A. K. Majumdar, B. M. Sadler, and Z. Xu, "Correction to "Modeling of non-line-of-sight ultraviolet scattering channels for communication"," *IEEE J. Select. Areas Commun.*, vol. 29, no. 1, pp. 250–250, Jan. 2011.

[28] Y. Zuo, H. Xiao, J. Wu, W. Li, and J. Lin, "Closed-form path loss model of non-line-of-sight ultraviolet single-scatter propagation," *Opt. Lett.*, vol. 38, pp. 2116–2118, Dec. 2013.

[29] C. Gong and Z. Xu, "Channel estimation and signal detection for optical wireless scattering communication with inter-symbol interference," *IEEE Trans. Wireless Commun.*, vol. 14, no. 10, pp. 5326–5337, Oct. 2015.

[30] C. Gong and Z. Xu, "LMMSE SIMO receiver for short-range non-line-of-sight scattering communication," *IEEE Trans. Wireless Commun.*, vol. 14, no. 10, pp. 5338–5349, Oct. 2015.

[31] C. Gong and Z. Xu, "Non-line of sight optical wireless relaying with the photon counting receiver: A count-and-forward protocol," *IEEE Trans. Wireless Commun.*, vol. 14, no. 1, pp. 376–388, Jan. 2015.

[32] L. Rabiner and B. Juang, "An introduction to hidden Markov models," *IEEE ASSP Mag.*, vol. 3, no. 1, pp. 4–16, Jun. 1986.

[33] Y. Ephraim and N. Merhav, "Hidden Markov processes," *IEEE Trans. Inf. Theory*, vol. 48, no. 6, pp. 1518–1569, Jun. 2002.

[34] T. K. Moon, "The expectation-maximization algorithm," *IEEE Signal Processing Mag.*, vol. 13, no. 6, pp. 47–60, Nov. 1996.

[35] A. P. Dempster, N. M. Laird, and D. B. Rubin, "Maximum likelihood from incomplete data via the EM algorithm," *J. Royal Statist. Soc. Series B (methodological)*, vol. 39, pp. 1–38, 1977.
[36] G. D. Forney, "The viterbi algorithm," *Proc. IEEE*, vol. 61, no. 3, pp. 268–278, Mar. 1973.
[37] L. Bahl, J. Cocke, F. Jelinek, and J. Raviv, "Optimal decoding of linear codes for minimizing symbol error rate (corresp.)," *IEEE Trans. Inf. Theory*, vol. 20, no. 2, pp. 284–287, Feb. 1974.
[38] J. Hagenauer, E. Offer, and L. Papke, "Iterative decoding of binary block and convolutional codes," *IEEE Trans. Inf. Theory*, vol. 42, no. 2, pp. 429–445, Feb. 1996.
[39] S. Benedetto, D. Divsalar, G. Montorsi, and F. Pollara, "A soft-input soft-output APP module for iterative decoding of concatenated codes," *IEEE Commun. Lett.*, vol. 1, no. 1, pp. 22–24, Jan. 1997.
[40] M. Yang, W. E. Ryan, and Y. Li, "Design of efficiently encodable moderate-length high-rate irregular LDPC codes," *IEEE Trans. Commun.*, vol. 52, no. 4, pp. 564–571, Apr. 2004.
[41] M. P. Fossorier, "Quasicyclic low-density parity-check codes from circulant permutation matrices," *IEEE Trans. Inf. Theory*, vol. 50, no. 8, pp. 1788–1793, Aug. 2004.
[42] J. Chen, A. Dholakia, E. Eleftheriou, M. P. Fossorier, and X.-Y. Hu, "Reduced-complexity decoding of LDPC codes," *IEEE Trans. Commun.*, vol. 53, no. 8, pp. 1288–1299, Aug. 2005.